

HIGH-WAVENUMBER SOLAR *f*-MODE STRENGTHENING PRIOR TO ACTIVE REGION FORMATION: THE CASE OF ACTIVE REGIONS 11130, 11158, 11768, AND 12051

NISHANT K. SINGH¹, HARSHA RAICHUR¹, & AXEL BRANDENBURG^{1,2,3,4}

¹Nordita, KTH Royal Institute of Technology and Stockholm University, Roslagstullsbacken 23, SE-10691 Stockholm, Sweden

²JILA and Department of Astrophysical and Planetary Sciences, University of Colorado, Boulder, CO 80303, USA

³Department of Astronomy, AlbaNova University Center, Stockholm University, SE-10691 Stockholm, Sweden

⁴Laboratory for Atmospheric and Space Physics, University of Colorado, Boulder, CO 80303, USA

December 3, 2024, Revision: 1.206

ABSTRACT

We report a systematic strengthening of the local solar surface mode, i.e. the *f*-mode, 1–2 days prior to the emergence of an active region (AR) in the same (corotating) location while no indication can yet be seen in the magnetograms. Our study is motivated by earlier numerical findings of Singh et al. (2014) which showed that, in the presence of a nonuniform magnetic field that is concentrated a few scale heights below the surface, the *f*-mode fans out in the diagnostic $k\omega$ diagram at high wavenumbers. Here we explore this possibility using data from the Helioseismic and Magnetic Imager on board the *Solar Dynamics Observatory*, and show for four ARs 11130, 11158, 11768, and 12051, that at large latitudinal wavenumbers (corresponding to horizontal scales of around 3000 km), the *f*-mode displays strengthening about two days prior to AR formation and thus provides a new precursor for AR formation. The idea that the *f*-mode is perturbed days before any visible magnetic activity occurs on the surface can be important in constraining dynamo models aimed at understanding the global magnetic activity of the Sun.

Subject headings: Sun: dynamo — Sun: helioseismology — Sun: surface magnetism — turbulence

1. INTRODUCTION

Recent work has demonstrated the potential usefulness of employing the surface or fundamental *f*-mode in local helioseismology for detecting subsurface solar magnetism (Hanasoge et al. 2008; Daifallah et al. 2011; Felipe et al. 2012, 2013). While turbulence generally tends to lower the *f*-mode frequency (Fernandes et al. 1992; Murawski & Roberts 1993a; Duvall et al. 1998) relative to its theoretical value given by $\omega_f = \sqrt{gk}$, where g is the gravitational acceleration and k is the horizontal wavenumber, horizontal magnetic fields can increase the frequency (Murawski & Roberts 1993b), while vertical or inclined fields lead to a nonuniform behavior, depending on the value of the horizontal wavenumber (Singh et al. 2015). More importantly, however, horizontal *variability* of the subsurface magnetic field leads to a fanning of the *f*-mode, where changes in the integrated mode amplitude and position give clues about the depth of such a field (Singh et al. 2014). While these investigations demonstrated a number of previously unknown effects of the *f*-mode, they were restricted to idealizing conditions of an isothermal layer. In this Letter, we use observations with the Helioseismic and Magnetic Imager (HMI) on board the *Solar Dynamics Observatory* to search for possible similarities between observations and simulations.

We focus on the possibility of using changes in the *f*-mode to predict the emergence of active regions (ARs) days before they can be seen in magnetograms. Owing to the very nature of the *f*-mode being confined to the proximity of the surface, our approach is most sensitive to magnetic fields at shallow depths of just a few megameters (Mm), and ceases to be sensitive when the AR begins to become fully developed. Earlier at-

tempts of predicting the emergence of ARs employed time-distance seismology using *p*-modes and have suggested the occurrence of perturbations at larger depths of 40–75 Mm (Ilonidis et al. 2011; Kholikov 2013). On the other hand, the rising flux tube scenario suggests a retrograde flow at a depth of 30 Mm (Birch et al. 2010), which has however not been observed. Also morphological studies in the case of AR 11313 have suggested incompatibilities with the rising flux tube model (Getling et al. 2016). By contrast, in the distributed dynamo scenario (Brandenburg 2005), magnetic flux concentrations form spontaneously near the surface (Brandenburg et al. 2011, 2013), which might explain the aforementioned field concentrations at shallower depths. Spontaneous surface flux concentrations have also been seen in the deep hydromagnetic convection simulations of Stein & Nordlund (2012), where an unstructured magnetic field is allowed to enter the bottom of their computational domain. Such near-surface magnetic concentrations are expected to affect the *f*-mode as its eigenfunction peaks only a few Mm below the solar surface (cf. Schou 1999). It is possible that these perturbations could manifest themselves through detectable signatures.

Readers familiar with the conventional picture of buoyant flux tube emergence (e.g., Charbonneau 2010) might be concerned about depths as shallow as just a few Mm, because buoyant tubes of several kilogauss would reach the surface within an hour (~ 3 hours from the depth of 7.5 Mm in the simulations of Cheung et al. 2010), but this picture ignores the formation process and implants flux tubes as alien objects within the turbulent convection zone. By contrast, ARs and sunspots might instead be generated by the subsurface turbulence in ways similar to what has so far only been seen in idealized simulations (Brandenburg et al. 2013; Warnecke et al. 2013;

Mitra et al. 2014). The point here is not to defend this idea, but to raise awareness of alternative viewpoints that would facilitate the understanding of our results presented below.

Once the AR has been detected in magnetograms and becomes fully developed, the f -mode amplitude begins to be suppressed. This might be explained by the fact that the interaction of both f - and p -modes with ARs or sunspots leads to mode conversion, resulting in the absorption of mode power (Thomas, et al. 1982; Cally et al. 1994; Cally & Bogdan 1997). This would explain the observed reduction of the mode amplitude *after* the analyzed AR has been formed. However, what was not discussed earlier is that the mode amplitude from the same region can undergo a *transient* growth phase prior to the actual flux emergence. This exhibits a nonmonotonic temporal variation in the normalized mode power which first rises, reaches a maximum value a few days before there is any sign of flux emergence, and then decreases as the strength of the magnetic field in the same region increases. Although a proper explanation of this is not yet available, one might speculate that this could also be due to some kind of scattering, whereby p -modes would scatter off the magnetic flux concentrations and leak into enhanced f -mode power.

2. DATA ANALYSIS

We use line-of-sight Dopplergrams and magnetograms from observations with HMI in the cylindrical equal-area or Postel projection mappings that are publicly available on the Stanford website¹. Our analysis is based on 45 seconds cadence data with a projection scale of 0.03° per pixel, where the data represent the line-of-sight Doppler velocity $v(x, y, t)$. For each of the regions of interest, we consider a patch of 512^2 pixels covering an area of about $(180 \text{ Mm})^2 \approx (15^\circ)^2$ on the solar surface. We track these patches for several days using a frame of reference corotating with the mean (Carrington) rotation rate Ω_0 with $\Omega_0/2\pi = 424 \text{ nHz}$. To capture transient signatures, we use data cubes $v(x, y, t)$ of only 8 hours duration for the entire tracking period of our target region. To reduce the noise level arising from solar convection (Zhao et al. 2015) and effects from latitudinal differential rotation (J. Zhao, private communication), we use a running difference to the original images before storing $v(x, y, t)$.

We divide our five or six day stretches into 15 or 18 intervals of 8 hrs, resulting in a data cube of $512^2 \times 640$ points of $v(x, y, t)$ that is Fourier transformed to give $\hat{v}(k_x, k_y, \omega)$, which too has the dimension m s^{-1} in our normalization. We then construct power spectra from $P = |\hat{v}|^2$ and select $k_x = 0$ in the subsequent analysis. Thus, we ignore longitudinal variations that could be affected by the cylindrical equal-area projection, because the latitudinal directions are expected to be the least affected. Also, our target regions were chosen such that the patches were always far from the limb during the entire tracking period. The thus obtained power spectra $P(k_x = 0, k_y, \omega)$ are then used to construct a diagnostic $k\omega$ diagram in the k_y - ω plane; see Figure 1(a) which displays the f - and p -ridges where the horizontal wavenumber is $k = k_y$.

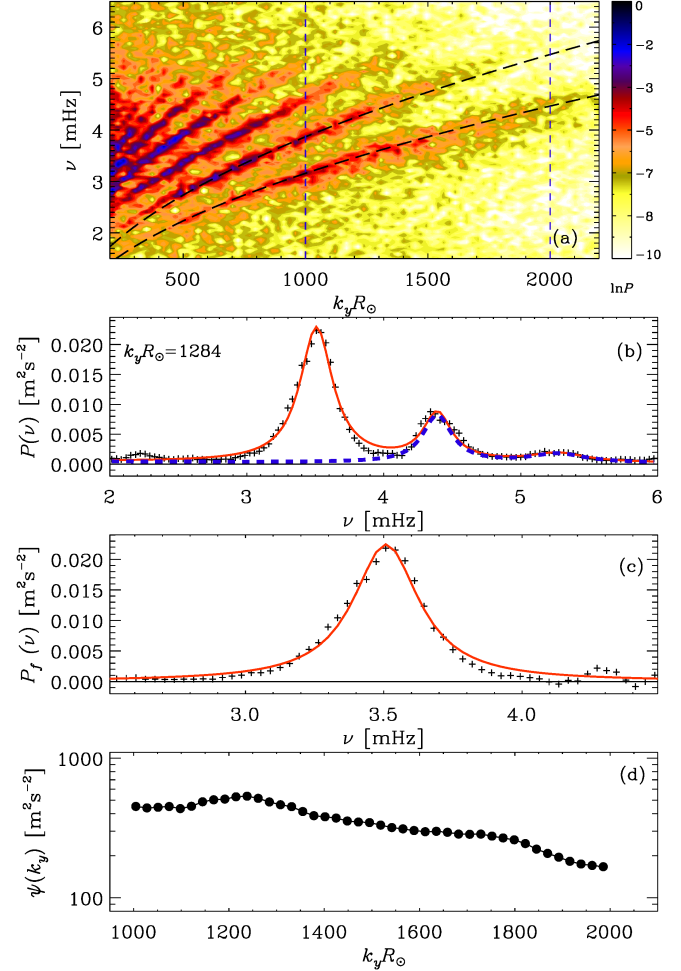


FIG. 1.— (a) Typical $k\omega$ diagram where the lowest ridge is the f -mode; (b) example of a vertical cut at a specified $k_y R_\odot$ (plus symbols) together with the model fit (solid, red curve) and P_{cp} (dashed, blue line); (c) f -mode ridge (P_f , plus symbols) and the corresponding fit (solid, red curve); (d) $\psi(k_y)$ for the full range enclosed within the vertical dashed lines in (a).

We now take a cut parallel to the frequency axis at a fixed $k_y R_\odot$ to get the line profiles of the f - and lowest two p -ridges. We then apply boxcar smoothing along the frequency axis with a box width of 0.24 mHz . To determine the strength of the f -mode, we remove the continuum and the lowest two p -ridges, which are represented by a superposition of parabolic and Lorentzian fits, respectively and denoted by $P_{\text{cp}} = |\hat{v}|_{\text{cp}}^2$, where the subscript cp stands for the sum of continuum and p -modes; see Figure 1(b) and (c). In most cases we repeat the same procedure at all wavenumbers in the range $k_y R_\odot \in [1200, 2000]$, and determine the f -mode power as $P_f(k_y, \omega) = |\hat{v}_f|^2 = P - P_{\text{cp}}$. We may define the integrated f -mode amplitude assuming circularly symmetric rings in the k_x - k_y plane as

$$\langle v^2 \rangle_f = 2AT \int_0^\infty \int_0^\infty k P_f(k, \omega) \frac{dk}{2\pi} \frac{d\omega}{2\pi}, \quad (1)$$

which we write as

$$\langle v^2 \rangle_f = L \sum_k k P_{f,k} \text{ with } P_{f,k} = 2 \sum_\omega P_f(k, \omega), \quad (2)$$

¹ <http://jsoc.stanford.edu/>

where $A = L^2$ is the area of the chosen patch, L is the side length and T is the tracking time of the data cube. Thus, we can determine the energy of the f -mode, E_f , characterizing its strength, as:

$$E_f(t) \equiv \frac{1}{2} \langle v^2 \rangle_f(t) = \frac{1}{2} \left(\frac{L}{R_\odot} \right) \sum_k \psi(k) \quad (3)$$

with $\psi(k) = kR_\odot P_{f,k}$; see Figure 1(d) and note that we determine the above quantities by setting $k_x = 0$. The time dependence of E_f may now be determined by computing the above quantities from the sequence of 8 h data cubes prepared for all tracked regions of interests.

In the quiet phase, say, during solar minimum, E_f shows a systematic dependence on the angular distance α from the disk center, given by

$$\cos \alpha = \cos \vartheta \cos \varphi; \quad \varphi = \varphi_* - \varphi_0 + \Omega_{\text{syn}} t, \quad (4)$$

with ϑ and φ being respectively the latitude and longitude of the point of interest, φ_* is the corresponding Carrington longitude, φ_0 is the Carrington longitude of the disk center at the time when we began tracking the target patch, and $\Omega_{\text{syn}} = 2\pi/27.275$ days is the mean synodic Carrington rotation rate of the Sun (i.e., the apparent rotation rate as viewed from the Earth).

As suggested by earlier work (Singh et al. 2014), we focus on E_f for fairly large k_y . We track a particular position on the solar surface in time t using the average (Carrington) rotation rate. Normalizing by the solar radius $R_\odot = 700$ Mm gives the spherical harmonic degree $k_y R_\odot$. For a fixed range of $k_y R_\odot$, we compute the dependence of E_f on t . Empirically, the value of E_f of the quiet Sun (the position where no AR emerges within the next few days) shows a systematic variation that is approximately of the form $\zeta(\cos \alpha) = \cos \alpha(1 + 0.72 \cos \alpha)$. We therefore define

$$\tilde{E}_f \equiv E_f / \zeta, \quad (5)$$

which fluctuates moderately about some average value in the quiet phase of the Sun. However, several days *prior* to the emergence of an AR, our studies show elevated values of \tilde{E}_f at that corotating patch where this AR later emerges.

It is useful to make a simultaneous comparison with the value for relatively quiet Sun patches under otherwise identical local conditions. This may be realized as follows: corresponding to each target region at (ϑ, φ) , we consider a (quiet) mirror region at $(\vartheta^\dagger, \varphi)$ in the opposite hemisphere with the same dimensions, and track both these patches simultaneously, where $\vartheta^\dagger = -\vartheta$ for the entire tracking period. We refer to this value as \tilde{E}_f^\dagger . We confirm that, while the rms magnetic field B_{rms} rises when the AR emerges, the value in the mirror region, B_{rms}^\dagger , remains close to a constant background value.

3. RESULTS

In Figures 2 and 3 we show for four ARs (11130, 11768, 11158, and 12051) the time traces of \tilde{E}_f for corotating patches at which later the ARs emerge and compare with those of the mirror regions \tilde{E}_f^\dagger (top rows), the rms magnetic field B_{rms} within those patches (second rows), and the corresponding full disk line-of-sight magnetograms

at $t = t_{\text{AR}} - 2$ d (third rows) and at $t = t_{\text{AR}}$ (last rows), which are the times when the ARs emerge and were assigned their numbers. All four ARs show similar characteristics: an early rise of \tilde{E}_f with a maximum 1–2 days prior to t_{AR} , followed by a decline at and after t_{AR} , as well as a delayed increase of \tilde{E}_f^\dagger , sometimes with a maximum near t_{AR} . By contrast, during a suitably chosen time in 2010, the Sun was nearly completely quiet, and both \tilde{E}_f and \tilde{E}_f^\dagger follow each other rather closely (Figure 4), although their time traces show still considerable variability. This might be caused by subsurface turbulence and small-scale magnetic fields even for the quiet Sun, or perhaps by instrumental effects. The fact that \tilde{E}_f and \tilde{E}_f^\dagger remain close to each other at all times shows that in the quiet phase of the Sun, the integrated f -mode amplitudes in the two hemispheres evolve *symmetrically*, so that the difference is small and therefore not significant. Note also that, since no AR has emerged during that time, we replaced t_{AR} in this figure by the time of central meridian crossing t_{CM} of an arbitrarily chosen comoving patch.

Based on these findings, the following hypotheses may be formulated. In regions with low or no surface magnetic activity, a nearly flat time trace without systematic differences between \tilde{E}_f and \tilde{E}_f^\dagger suggests low subsurface magnetic activity while a gradual and systematic enhancement of \tilde{E}_f relative to \tilde{E}_f^\dagger is suggestive of a build-up of subsurface magnetic activity. In already established ARs, on the other hand, \tilde{E}_f is visibly depressed and \tilde{E}_f^\dagger may or may not show a marked rise, depending on the complexity of the already established surface activity.

Let us now discuss the individual examples in more detail. AR 11130 was a solitary AR during 2010 when the overall solar activity was still rather low. It is therefore an example where interference from other locations on the Sun is minimal. Indeed, it shows most strikingly the “symmetry breaking” between \tilde{E}_f and \tilde{E}_f^\dagger , with \tilde{E}_f showing a maximum about 1.5 days before this AR emerges.

For AR 11768, there is again the characteristic symmetry breaking between \tilde{E}_f and \tilde{E}_f^\dagger , but in this case the initial rise is sharper than for AR 11130. This is to some extent caused by strongly diminished mode strength for larger k , which led us to choose a narrower k interval in the analysis, $k_y R_\odot \in [1200, 1300]$. This explains also the lower integrated mode strength in the top right panel of Figure 2. This provides a hint of a possible wavenumber dependence of the effect causing the f -mode strengthening prior to AR formation and will be studied elsewhere.

Next, we consider AR 11158, which was a rapidly growing AR that produced the first X-class flare of solar cycle 24 on 2011 February 15 (Maurya et al. 2012) with an Earth-directed halo coronal mass ejection (Schrijver et al. 2011). It also produced several M-class flares during February 13–16 (Inoue et al. 2013), after being designated its number on February 12. Also in this case, \tilde{E}_f shows a clear increase with $\tilde{E}_f - \tilde{E}_f^\dagger \sim 150 \text{ m}^2 \text{s}^{-2}$ about a day before B_{rms} reaches a plateau of about 220 G. The energy increase of about $\sim 200 \text{ m}^2 \text{s}^{-2}$ seen about three days prior to the AR emergence appears to be indicative of the subsurface concentration of the

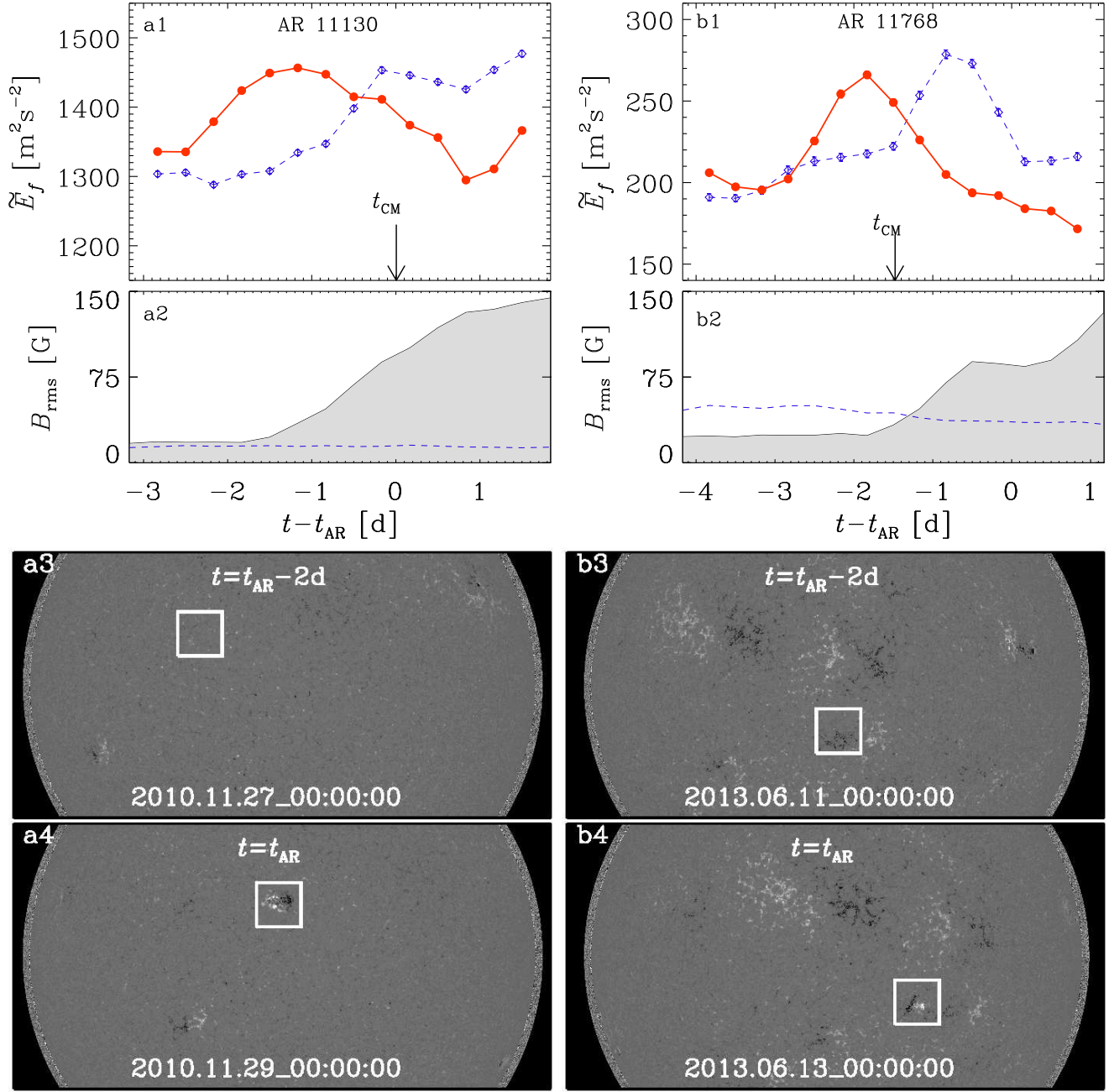


FIG. 2.— Time traces of \tilde{E}_f (solid red line) and \tilde{E}_f^\dagger (dashed blue line) as a function of $t - t_{\text{AR}}$, with t_{CM} marking the time of central meridian crossing (top row), B_{rms} (solid line with shaded area underneath) together with B_{rms}^\dagger (dashed blue line) as a function of $t - t_{\text{AR}}$ (second row), as well as magnetograms at $t = t_{\text{AR}} - 2\text{d}$ (third row) and $t = t_{\text{AR}}$ (bottom row) for AR 11130 (left) and AR 11768 (right).

magnetic field resulting in a rapid growth of B_{rms} at the photosphere. Thus, the same general trend is found here too, although the potential for using $\tilde{E}_f(t)$ as a precursor was less clear in the sense that it showed a maximum only about a day in advance. The subsequent increase in E_f^\dagger is noticeable here as well.

We now turn to the case of AR 12051, which lies next to bigger and stronger ARs that had appeared already in the southern hemisphere; see the magnetograms in the right-hand panels of Figure 3. Here too we find that the evolution of \tilde{E}_f obtained from the patch where later

AR 12051 emerges is not flat. It rises from a level of about $\sim 1200 \text{ m}^2 \text{s}^{-2}$ and attains a maximum value $\sim 1400 \text{ m}^2 \text{s}^{-2}$ more than two days before it was designated its number on 2014 May 2 and nearly three days before B_{rms} reached its maximum value of about 150 G. On May 3, this AR developed a so-called δ -class spot with M class flares a few days later. However, the essential difference here is that the \tilde{E}_f^\dagger from the relatively quiet mirror patch remains larger than \tilde{E}_f at all times. This may be understood as follows: as the southern hemisphere is already ‘polluted’ by many ARs, the f -mode is expected to be

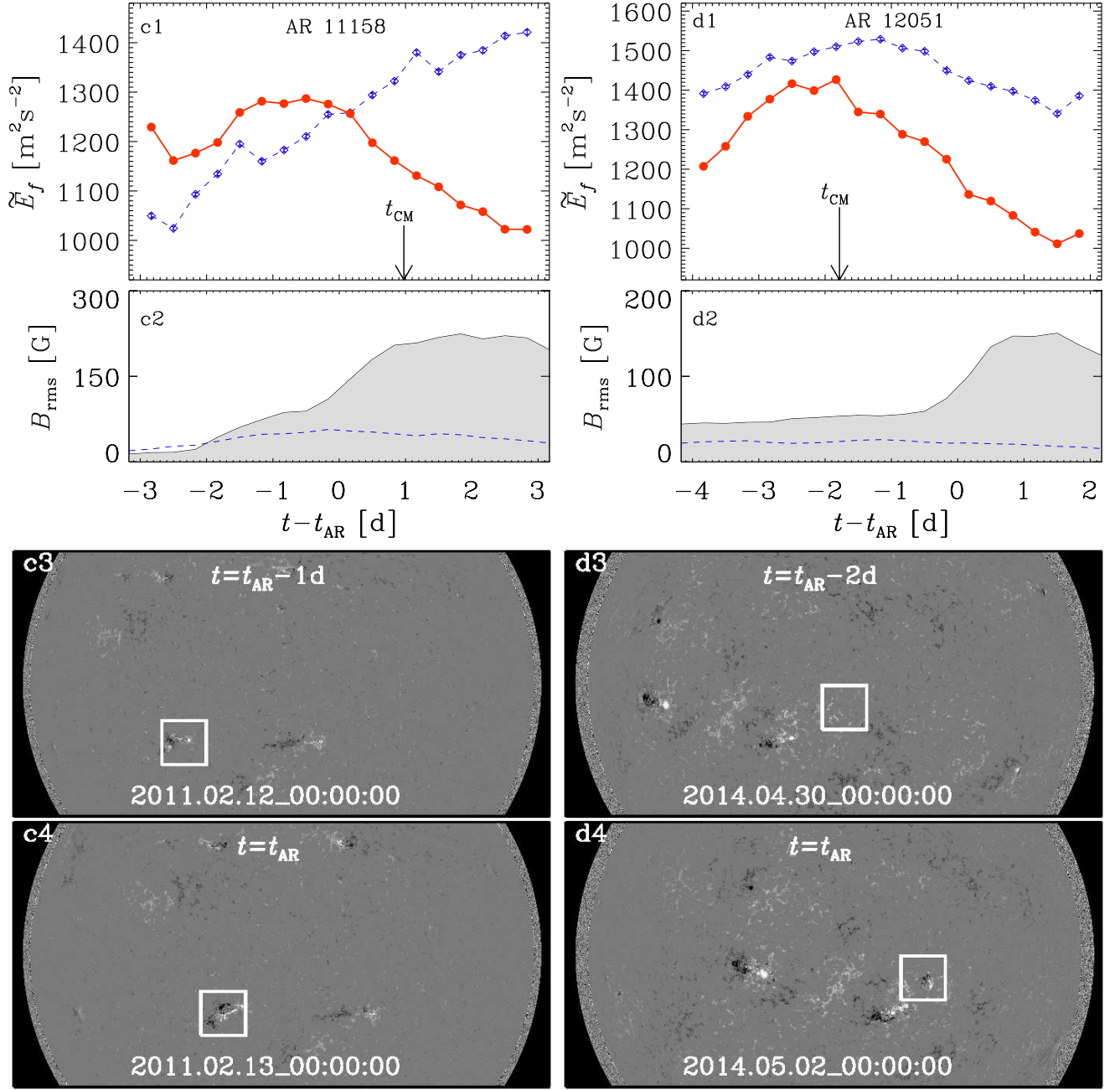


FIG. 3.— Same as Figure 2, but for AR 11158 (left) and AR 12051 (right).

damped in this hemisphere and therefore the time-trace of \tilde{E}_f for AR 12051, while showing early precursor signatures, does not overcome \tilde{E}_f^\dagger from the northern hemisphere where the f -mode remains undamped and shows a much smaller variation.

All four examples presented above show that several days prior to magnetic field emergence the strength of the f -mode, as presented by the value of \tilde{E}_f , rises and then reaches a maximum before showing the known post-emergence damping. Also, prior to AR emergence, the value of \tilde{E}_f remains larger for long times with significant energy difference compared to the value obtained from the corresponding quiet Sun location, $(\vartheta^\dagger, \varphi)$. For

AR 12051, however, this is different and, as explained earlier, the reason for this is in fact expected.

As an important extension of this work, we now also calculate images of \tilde{E}_f for the solar disk. This gives the most direct information of where the next AR might form; see Figure 5. Although we see a moderate degree of fluctuations, there are also systematic effects—especially near the limb. These may be caused by instrumental effects such as variations of the modulation transfer function (Wachter et al. 2012). The remaining variations may either also be related to instrumental effects or they could be caused by weaker subsurface magnetic fields that must always be present—even during

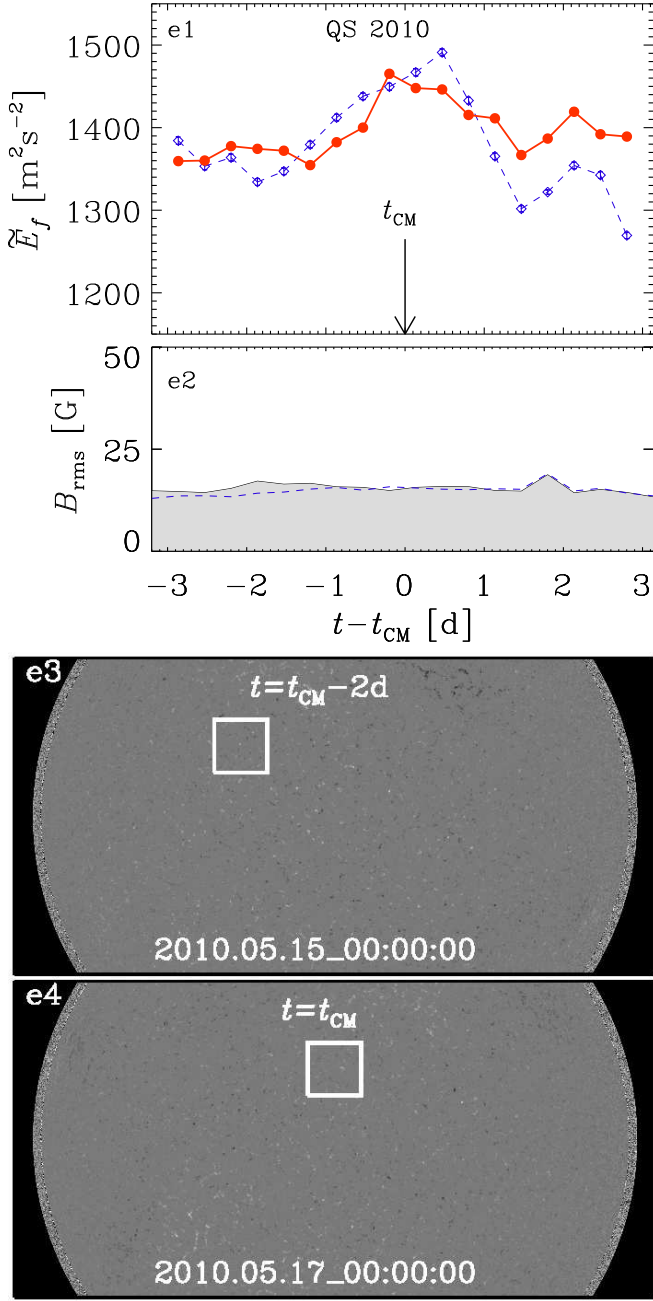


FIG. 4.— Same as Figure 2, but for the quiet Sun around 2010 May 17. Solid (red) and dashed (blue) lines correspond to $\vartheta = +20^\circ$ and -20° , respectively.

solar minimum.

It would be interesting to see whether there are other indicators, for example in the magnetic field itself, which could also give early indications of AR formation. We emphasize, however, that the maximum of $|B|$ shows an onset only at the same time as B_{rms} does, which is therefore too late.

4. IMPLICATIONS

If we accept that $\tilde{E}_f(t)$ can be used as a precursor to AR formation, we must ask about its possible physical origin and relevance. Earlier idealized simulations (Singh et al. 2014, 2015) have demonstrated that, while

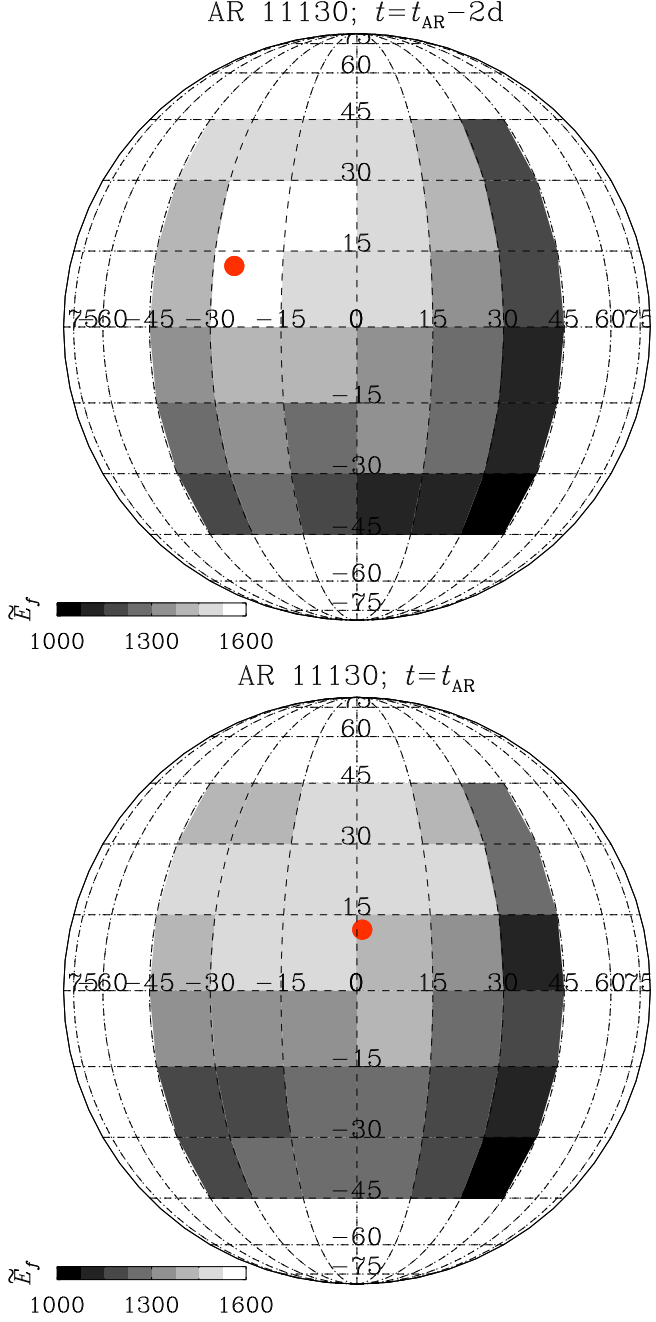


FIG. 5.— Magnetograms and images of \tilde{E}_f for a relatively quiet phase of the Sun in 2010 when an isolated AR 11130 emerged on 2010 November 29. Left: top and bottom panels show the magnetograms at $t = t_{AR} - 2d$ and $t = t_{AR}$, respectively. Middle and right: images of \tilde{E}_f two days before the AR emergence and at $t = t_{AR}$, respectively. Red filled circle denotes the location of AR 11130.

uniform magnetic fields lead to a frequency shift and a weakening of the f -mode, a nonuniform subsurface field can lead to a fanning and associated strengthening of the f -mode, provided the magnetic field is at least one or two pressure scale heights below the surface. While such studies should be repeated with more realistic models, they do confront us with the question of how a magnetic field can remain undetected once it is only a few Mm below the surface.

The fact that the *f*-mode resides near the top few Mm of the Sun is suggestive of a gradual build-up of the AR near the surface, instead of a buoyant rise, which would happen in just a few hours (Cheung et al. 2010). This is in stark contrast to the conventional picture of an Ω -shaped flux tube rising from the bottom of the convection zone and forming an AR as it pierces the surface (Fan 2001). Earlier simulations of Cheung et al. (2010) with a magnetic field implanted at a depth of nearly 10 Mm below the surface have produced surface manifestations just a few hours later. Such simulations do not address the physics of the *formation* of magnetic flux concentrations. By contrast, several simulations in large enough domains performed by several groups (Stein & Nordlund 2012; Warnecke et al. 2013;

Mitra et al. 2014) have demonstrated the spontaneous emergence of magnetic flux concentrations right at the surface. This highlights the potential significance of *f*-mode related precursors at constraining our still very sketchy understanding of the solar dynamo (Ossendrijver 2003; Brandenburg 2005; Charbonneau 2010).

REFERENCES

Birch, A. C., Braun, D. C., & Fan, Y. 2010, *ApJ*, 723, L190
 Brandenburg, A. 2005, *ApJ*, 625, 539
 Brandenburg, A., Kemel, K., Kleeorin, N., Mitra, D., & Rogachevskii, I. 2011, *ApJ*, 740, L50
 Brandenburg, A., Kleeorin, N., & Rogachevskii, I. 2013, *ApJ*, 776, L23
 Cally, P. S., Bogdan, T. J., & Zweibel, E. G. 1994, *ApJ*, 437, 505
 Cally, P. S., & Bogdan, T. J. 1997, *ApJ*, 486, L67
 Charbonneau, P. 2010, *Living Rev. Solar Phys.*, 7, 3
 Cheung, M. C. M., Rempel, M., Title, A. M., & Schüssler, M. 2010, *ApJ*, 720, 233
 Daiffallah, K., Abdellatif, T., Bendib, A., Cameron, R., & Gizon, L. 2011, *Solar Phys.*, 268, 309
 Duvall, T. L., Jr., Kosovichev, A. G., & Murawski, K. 1998, *ApJ*, 505, L55
 Fan, Y. 2001, *ApJ*, 554, L111
 Felipe, T., Braun, D., Crouch, A., & Birch, A. 2012, *ApJ*, 757, 148
 Felipe, T., Crouch, A., & Birch, A. 2013, *ApJ*, 775, 74
 Fernandes, D. N., Scherrer, P. H., Tarbell, T. D., & Title, A. M. 1992, *ApJ*, 392, 736
 Getling, A. V., Ishikawa, R., & Buchnev, A. A. 2016, *Solar Phys.*, 291, 371
 Hanasoge, S. M., Birch, A. C., Bogdan, T. J., & Gizon, L. 2008, *ApJ*, 680, 774
 Ilonidis, S., Zhao, J., & Kosovichev, A. 2011, *Science*, 333, 993
 Inoue, S., Hayashi, K., Shiota, D., Magara, T., & Choe, G. S. 2013, *ApJ*, 770, 79
 Kholikov, S. 2013, *Solar Phys.*, 287, 229
 Maurya, R. A., Vemareddy, P., & Ambastha, A. 2012, *ApJ*, 747, 134
 Mitra, D., Brandenburg, A., Kleeorin, N., Rogachevskii, I. 2014, *MNRAS*, 445, 761
 Murawski, K. and Roberts, B. 1993a, *A&A*, 272, 601
 Murawski, K. and Roberts, B. 1993b, *A&A*, 272, 595
 Ossendrijver, M. 2003, *A&A Rev.*, 11, 287
 Schou, J. 1999, *ApJ*, 523, L181
 Schrijver, C. J., Aulanier, G., Title, A. M., Pariat, E., & Delannée, C. 2011, *ApJ*, 738, 167
 Singh, N. K., Brandenburg, A., & Rheinhardt, M. 2014, *ApJ*, 795, L8
 Singh, N. K., Brandenburg, A., Chitre, S. M., & Rheinhardt, M. 2015, *MNRAS*, 447, 3708
 Stein, R. F., & Nordlund, Å. 2012, *ApJ*, 753, L13
 Thomas, J. H., Cram, L. E., & Nye, A. H. 1982, *Nature*, 297, 485
 Wachter, R., Schou, J., Rabbelo-Soares, M. C., Miles, J. W., Duvall, T. L., & Bush, R. I. 2012, *Solar Phys.*, 275, 261
 Warnecke, J., Losada, I. R., Brandenburg, A., Kleeorin, N., & Rogachevskii, I. 2013, *ApJ*, 777, L37
 Zhao, J., Chen, R., Hartlep, T., & Kosovichev, A. G. 2015, *ApJ*, 809, L15